Short pitch corrugation mitigation by rail constraint design

Zhang, Pan; Li, Shaoguang; Li, Zili

DOI
10.1016/j.ijmecsci.2022.108037

Publication date
2023

Document Version
Final published version

Published in
International Journal of Mechanical Sciences

International Journal of Mechanical Sciences 243 (2023) 108037

Contents lists available at ScienceDirect

International Journal of Mechanical Sciences

journal homepage: www.elsevier.com/locate/ijmecsci

Short pitch corrugation mitigation by rail constraint design

Pan Zhang, Shaoguang Li, Zili Li *

Section of Railway Engineering, Delft University of Technology, Stevinweg 1, Delft, CN 2628, the Netherlands

ARTICLE INFO

Keywords:
Short pitch corrugation mitigation
Rail constraint design
Rail longitudinal compression modes
Longitudinal dynamic contact force
Operating deflection shapes
3D Fe vehicle-track dynamic interaction model

ABSTRACT

Short pitch corrugation is a quasi-periodic rail defect that induces a high level of noise and accelerates track degradation. This paper proposes a methodology to mitigate short pitch corrugation by rail constraint design, including four steps. In Step 1, corrugation is numerically reproduced by employing a three-dimensional (3D) finite element (FE) vehicle-track model with degraded fastenings. In Step 2, the corrugation initiation mechanism is identified by the operating deflection shapes (ODSs) approach. In Step 3, different types of rail constraints are designed and their effects on rail vibration modes are analysed. Then FE models of these rail constraints are built up and validated. In Step 4, rail constraint models from Step 3 are applied to the 3D FE vehicle-track interaction model and their effectiveness on corrugation mitigation is evaluated. The results indicate rail longitudinal compression modes and the induced longitudinal dynamic contact force dominate the initial differential wear and corrugation initiation. Based on this mechanism, a new rail constraint is designed in this work that can completely suppress longitudinal compression modes and significantly reduce the fluctuation amplitude of the longitudinal contact force so that corrugation can hardly initiate. This paper first points out a direction for field corrugation mitigation by strengthening the rail longitudinal constraint.

1. Introduction

Corrugation has been reported as a type of wary rail defect for over 100 years and remains a severe problem for railway administrations worldwide. According to different formation mechanisms, corrugation is mainly classified into six groups, heavy haul, light rail, booted sleeper, contact fatigue, rutting and short pitch corrugation, respectively [1]. This work focuses on short pitch corrugation on tangent tracks or gentle curves, and the term 'corrugation' below refers to this type of corrugation only. Corrugation has a typical wavelength of 20–80 mm [1,2], and it can be identified by shiny crests and dark valleys in the running band. One example of rail corrugation in the Dutch Railway is shown in Fig. 1, with a wavelength of about 40 mm. The field observation shows in the Netherlands 74% of squats are related to corrugation [3]. It is noted that these data are not the statistical data of the whole Dutch railway network and may depend on the maintenance measures such as grinding. Corrugation can excite high-frequency wheel-rail contact forces [4,5] and generate a high level of noise [6–8], for which it is often referred to as 'roaring rails' [1]. In addition, the resulting dynamic contact forces will accelerate the degradation of the track component [9], such as fastenings, sleepers and ballast, and lead to other types of rail defects, e.g., squats [10]. In practice, rail grinding has been widely applied to treat corrugation [11–13]. For the guidance of field grinding maintenance, some novel inspection approaches of corrugation have been proposed, for instance, based on the self-contained electromagnetic energy harvesting system [14], carriage interior noise [15], or one-dimensional convolution neural network and data-driven method [16]. However, grinding considerably increases the maintenance cost and meanwhile reduces the service life of the rail. Therefore, it is of great significance to identify the corrugation formation mechanism and develop effective root-cause solutions to prevent corrugation.

The corrugation formation mechanism is generally considered to consist of two features: the wavelength-fixing mechanism and the damage mechanism [1,2]. Corrugation damage mechanism has been commonly considered as wear [12,17–22]. A well-validated wavelength-fixing mechanism has not yet been demonstrated, although many hypotheses have been proposed in the literature. Hempelmann and Knothe [23] and Muller [24] employed the linear wheel-track model to predict the corrugation formation and found that the track pinned-pinned resonance together with the contact filter effect are the wavelength-fixing mechanisms. Afferrante and Ciavarella [25] reported that the influence of pinned-pinned resonance has been possibly overestimated and first proposed the longitudinal creepage may be the most important mechanism without corresponding to any resonance of the

* Corresponding author.
E-mail address: z.li@tudelft.nl (Z. Li).

https://doi.org/10.1016/j.ijmecsci.2022.108037
Received 3 October 2022; Received in revised form 10 December 2022; Accepted 13 December 2022
Available online 14 December 2022

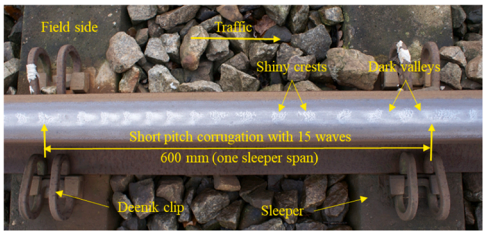

Fig. 1. Short pitch corrugation with a wavelength of about 40 mm in the Dutch railway network. Corrugation wavelength refers to the distance between two adjacent shiny crests. This corrugation is developed on a straight ballasted track with duo-block sleepers and fastenings with the Deennik clip. Less severer corrugation is found on the other rail at the same site.

vehicle-track system. Johansson and Nielsen [26] numerically studied the influence of powered wheelsets with wheel corrugation on the rail corrugation growth and found that the local rail bending modes between the two wheelsets in a bogie determine the corrugation wavelength. Wu and Thompson [27] and Ma et al. [28] also reported that the dynamic resonance between multiple wheelset-rail interactions can induce vertical wheel-rail dynamic force and be responsible for corrugation formation. Meehan et al. [17,29–31] performed numerical simulations and field and laboratory tests of rail corrugation, and concluded that train speed variation can significantly reduce the corrugation rate. Chen [32] and Cui [33] employed the finite element wheelset-track model to investigate the corrugation development mechanism and proposed that the frictional self-excited vibration of the wheelset-track system is responsible for the wavelength-fixing mechanism. Li et al. [34] conducted field measurement and numerical calculations to study corrugation formation on tracks with resilient fastenings and found corrugation arises by a wavelength-fixing mechanism of rail vertical resonance on the elasticity of resilient fastenings.

Despite the different or even contradictory theories in the literature, it is commonly accepted that the wavelength-fixing mechanism is mainly determined by the interplays of the structural dynamics and the contact mechanics. Therefore, the accurate modelling of high-frequency dynamics and wheel-rail contact of the vehicle-track system is essential to understand corrugation formation. With the development of computational power, the finite element model (FEM) has been extensively applied in simulating vehicle-track dynamic interaction. Compared to the multibody models [35,36] or beam models [37–39], the FEM has the advantage in dealing with nonlinear material properties and arbitrary contact geometry and inherently include continuum dynamics [40,41]. It thus has been used to investigate, e.g., wheel-rail impact contact [42,43], contact-induced waves [44], rail ratchetting [45,46], and railway curve squeal [47,48].

Employing a novel modelling approach based on the three-dimensional (3D) FE simulation of vehicle-track dynamic interaction, Li et al. [4] obtained new insights into the corrugation development mechanism. It was inferred that rail longitudinal vibration modes are probably dominant for corrugation initiation. Further, continuous corrugation initiation and growth require a consistency condition between the vertical and longitudinal vibration modes, dynamical responses and the resulting wear. According to these insights, together with a necessary initial excitation determined by fastening constraint, consistent corrugation initiation and growth have been successfully reproduced. The simulated corrugation achieved good agreement with the field corrugation in terms of the spatial distribution and major wavelength components [49]. These results point out a promising direction that rail corrugation can be mitigated or even eliminated by completely constraining longitudinal compression modes [50,51] to suppress corrugation initiation.

In railway tracks, fastenings impose major constraints on rail vibrations. Fastenings mainly consist of two components: railpads and clips. Railpads are made of resilient materials placed between the rail and the sleeper to reduce vibration and noise, and its dynamic properties are highly nonlinear [52–55]. Clips fix the rail to the sleeper to ensure that the rail remains attached to the sleeper under train loads. Railpads and clips together constrain the displacement of the rail in the vertical, longitudinal and lateral directions [56]. Many experimental and numerical studies indicate that fastenings play an important role in the corrugation formation [24,57–60]. Zhang et al. [61,62] systematically investigated rail vibration modes in three directions using the operating deflection shape (ODS) approach and reported that the fastenings constrain the longitudinal rail compression modes less strongly compared to those in the vertical and lateral directions. Therefore, it is necessary to design new rail constraint instead of the current fastenings to better suppress longitudinal compression modes to mitigate corrugation.

This paper proposes a methodology to mitigate corrugation by rail constraint design. Through this methodology, corrugation is numerically reproduced using a 3D FE vehicle-track interaction model and its initiation mechanism is identified by the ODS approach. Different types of rail constraints are designed and their effects on rail vibrations and corrugation mitigation are investigated. The structure of this paper is as follows. Section 2 describes the methodology of this paper, including numerical simulations and experimental investigation. Section 3 presents the simulated corrugation and identifies the corrugation initiation mechanism by the ODS approach. Section 4 investigates different rail constraint designs and their modelling methods. Section 5 evaluates the effectiveness of rail constraints on corrugation mitigation. Section 6 further discusses the results and possible future researches. The main conclusions are presented in Section 7.

2. Methodology

In this section, we describe a methodology for corrugation mitigation by rail constraint design, as shown in Fig. 2. This methodology includes four steps: (1) corrugation reproduction; (2) identification of corrugation initiation mechanism; (3) design and modelling of rail constraints; (4) evaluation of the designed rail constraints on corrugation mitigation. In Step 1, a 3D FE vehicle-track interaction model with degraded fastenings is employed to numerically reproduce corrugation. In Step 2, the ODS approach is applied to identify the corrugation development mechanism. In Step 3, different rail constraints are designed and their influences on rail vibration modes are analysed. Afterwards, models of these rail constraints are established and validated. In Step 4, the rail constraint models from Step 3 are applied to the FE vehicle-track model and their effectiveness on corrugation mitigation is evaluated.

2.1. 3D FE vehicle-track interaction model for corrugation reproduction

In this subsection, we introduce the 3D FE vehicle-track interaction model in detail in Section 2.1.1, which can comprehensively simulate the wheel-rail contact and high-frequency dynamics of the vehicle-track system. This model is used to reproduce corrugation by introducing an initial excitation from a degraded fastening model. The damage mechanism is assumed as wear, which is calculated by the approach provided in Section 2.1.2.

2.1.1. 3D FE vehicle-track interaction model

A 3D FE vehicle-track interaction model was built up for corrugation reproduction, as shown in Fig. 3. A Cartesian coordinate system was adopted in the model, where the axes X, Y, and Z were in the longitudinal (rolling), lateral and vertical directions. The vehicle was modelled by a wheel with the sprung mass of the car body and bogie supported by the primary suspension. The secondary suspension was not included because the vibration of the sprung mass on the secondary suspension mainly influences vehicle-track vibration at lower frequencies (usually below 10 Hz [63]), which is beyond the frequency range of corrugation. The wheel, rail and sleeper were modelled by 8-node solid elements

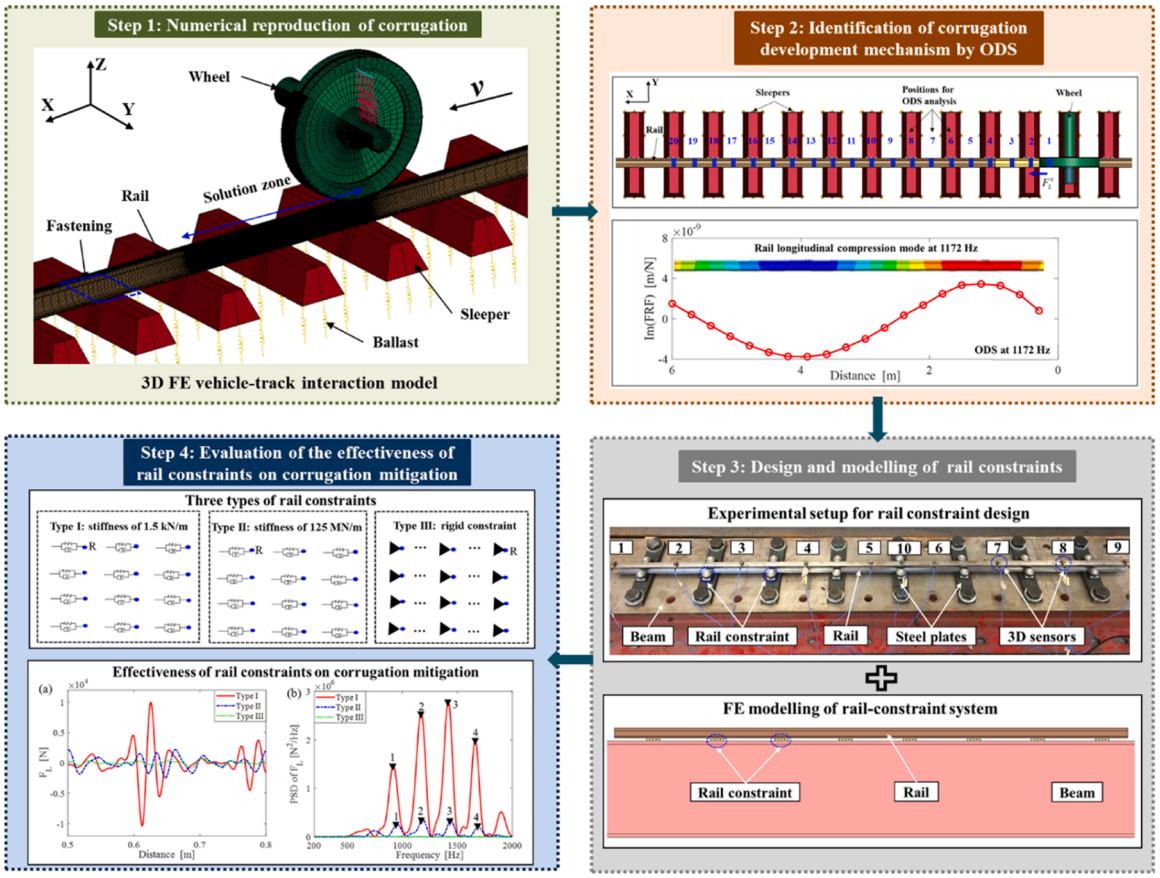

Fig. 2. Flowchart of the methodology for corrugation mitigation by rail constraint design. In Step 1, corrugation is numerically reproduced by employing a 3D FE vehicle-track interaction model. In Step 2, the corrugation development mechanism is identified by the ODS approach. In Step 3, different types of rail constraints are designed and modelled. In Step 4, the effectiveness of the designed rail constraints on corrugation mitigation is evaluated.

based on their nominal geometry and material. The radius of the wheel was 0.46 m with a conicity of 1/40. The rail profile was UIC 54 E1 with an inclination of 1/40. The primary suspension and ballast were modelled by vertical spring-damper elements. Fig. 3c shows a close-up of a degraded fastening model. Fastenings were modelled by vertical 3 × 4 spring-damper elements (i.e. 3 columns in the longitudinal dimension and 4 rows in the lateral). The lateral fastening constraint was modelled by rigidly fixing the rail nodes in all three columns, while the longitudinal one only rigidly constrained the rail in the central column to simulate the fastening degradation for corrugation initiation, compared to the three columns in the nominal fastening constraint [49]. The track length was 20.54 m, including 34 sleeper spans. The vehicle and track parameters were taken primarily from [4,64]. The wheel-rail contact model (see Fig. 3d) applied an automatic surface-to-surface contact scheme with a penalty contact algorithm [65]. The wheel-rail friction coefficient was 0.4. No geometric irregularities were applied to the wheel-rail contact surface. The solution zone had a meshing size of 0.8 mm×0.8 mm. The initial wheel position was at position *O*, as shown in Fig. 3d (0 m). The running speed is 140 km/h.

An implicit-explicit sequential approach was employed in the simulation to minimize the solution time and the dynamic effects during the initialization of wheel-rail interaction [40,66]. In the implicit calculation, the vehicle-track system reached an equilibrium state under gravity. The calculated nodal displacement was subsequently input as an initial condition of the explicit calculation of the vehicle-track dynamic interaction. In the explicit calculation, initial forward translation and rotation velocities were prescribed to the wheel model to generate rolling motion. The same initial translation velocity was applied to the car body and bogie. A driving torque was applied to the wheel axle as a load boundary condition to generate a traction coefficient of 0.15. The adopted integration time step was sufficiently small (79 ns) to ensure the stability of the integration and the contact.

This vehicle-track interaction model has been extensively validated in terms of frictional rolling contact solutions [40,41,66], wheel dynamics [67] and track dynamics [56]. The simulated dynamic responses of the vehicle-track system, such as axle box accelerations [68] and rail accelerations [67], have also achieved good agreement with measurements. Besides, this model has been employed to successfully identify the development mechanism of squats [43,69], and predict the contact-induced waves [44].

2.1.2. Wear model

The wear of the rail surface is assumed to be proportional to the accumulated frictional work during wheel passages [70,71]. In the FE simulation, the frictional work at each node is calculated for a wheel passage, i.e., from the node entering until leaving the contact patch as follows:

$$w(x,y) = kW_f(x,y) = k\sum_{i=1}^{N}\tau_i(x,y)v_i(x,y)\Delta t \quad (1)$$

where k is the wear coefficient, W_f (x, y) is the frictional work, τ_i (x, y) and v_i (x, y) are the local tangential stress and micro-slip, respectively, N the number of time steps Δt during which a node passes the contact patch.

2.2. ODS approach to identify corrugation initiation mechanism

In this work, the ODS approach is applied to identify rail vibration

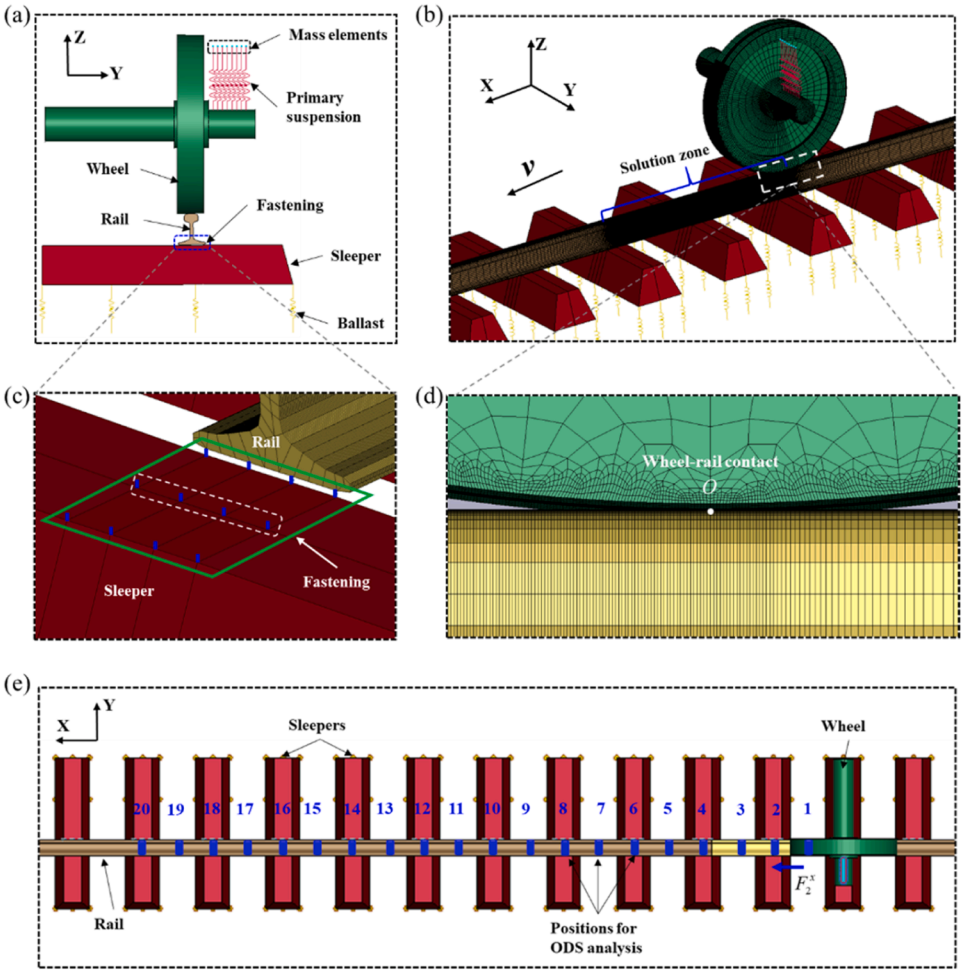

Fig. 3. 3D FE vehicle-track interaction model. (a) Front view; The car body and bogie were modelled as mass elements, the wheel, the rail and sleepers were modelled by 8-node solid elements, and the primary suspension, fastenings and the ballast were modelled by spring-damper elements. (b) detailed mesh of the FE model; The rail in the solution zone has the element size of 0.8 mm×0.8 mm. (c) close-up of the fastening model; Fastenings were modelled by vertical 3 × 4 spring-damper elements (i.e. 3 columns in the longitudinal dimension and 4 rows in the lateral). The fastening longitudinal constraint was only applied in the central column of rail nodes compared to the three columns in the nominal fastening constraint [49], as indicated by the white dashed box. (d) close-up of the wheel-rail contact; The initial wheel position was at position *O* (0 m). (f) top view; The vibration signal acquisition positions for ODS analysis are shown with numbers 1, 2, …, 20.

modes to understand the corrugation development mechanism. Compared to the widely-used frequency response function (FRF) approach [72,73], the ODS approach has the advantage in distinguishing coupled rail vibration modes [62]. ODS is calculated from a set of frequency response functions (FRFs), which can be divided into three steps. First, a longitudinal impact signal (denoted as $F_2^x(t)$) is applied at position 2 (see Fig. 3e), which is 0.6 m away from the origin position (*O*) and in the middle of the solution zone of corrugation. The vibration signals at 20 positions (see Fig. 3e) are captured and denoted as $a_i^x(t)$. Second, the FRFs at these positions are calculated by the following formula:

$$\mathrm{FRF}_i^x(f) = \frac{S_{a_i^x F_2^x}(f)}{S_{F_2^x F_2^x}(f)(2\pi f)^2} \tag{2}$$

where $\mathrm{FRF}_i^x(f)$ is the longitudinal FRF at position *i*, $S_{a_i^x F_2^x}$is the cross-spectrum between the acceleration $a_i^x(t)$, and force $F_2^x(t)$, and $S_{F_2^x F_2^x}$ is the auto-spectrum of the force $F_2^x(t)$. Third, the ODSs of rail displacement responses are taken as the spatial distribution of the imaginary parts of the FRFs, as follows:

$$\mathrm{ODS}^x(f) = \left[\mathrm{Im}\left(\mathrm{FRF}_1^x(f)\right),\ \mathrm{Im}\left(\mathrm{FRF}_2^x(f)\right), \ldots,\ \mathrm{Im}\left(\mathrm{FRF}_{20}^x(f)\right)\right] \tag{3}$$

where $\mathrm{ODS}^x(f)$ is the longitudinal ODS at frequency *f*. When the frequency is one of the natural rail frequencies, the ODS will closely approximate the mode shape. More detailed introduction of the ODS approach can be found in [61,62].

2.3. Design and modelling of rail constraints for corrugation mitigation

In this subsection, experimental setups with different types of rail constraints are introduced. Afterwards, FE models of these rail constraints are developed.

2.3.1. Experimental setups for rail constraint design

Fig. 4 shows the experimental setups for rail constraint design to mitigate corrugation. The experimental setups mainly consist of three parts (see Fig. 4a): a rail, a standard 'I-cross section' steel beam, and different types of rail constraints,. The rail is 1.6 m long and its profile is approximately 1/5 scale of the UIC 54 E1 rail but with some modifications for ease of fabrication, as shown in Fig. 4e. According to the similarity law [74,75], the vibration modes of a scaled rail are equivalent to those of the full-scale rail by considering a corresponding scale factor. Compared to the full-scale one, the downscaled rail is easier to control by rail constraints in the laboratory because of its much size. Besides, it is possible to experimentally examine the effectiveness of the designed rail constraint for corrugation mitigation in an innovative downscale test rig [75,76] in future work. The steel beam has a considerably larger mass and stiffness than the scaled rail, provides an approximately rigid support to the rail, and makes it possible to completely suppress rail vibration modes by rail constraints.

To control longitudinal compression modes, five types of rail constraints were designed, as shown in Fig. 4 and listed in Table 1. For the first type of rail constraint (type 1), the rail was supported on the steel beam by two soft styrofoam blocks at the two rail ends, as shown in Fig. 4b. In this condition, the rail can be approximately considered to be

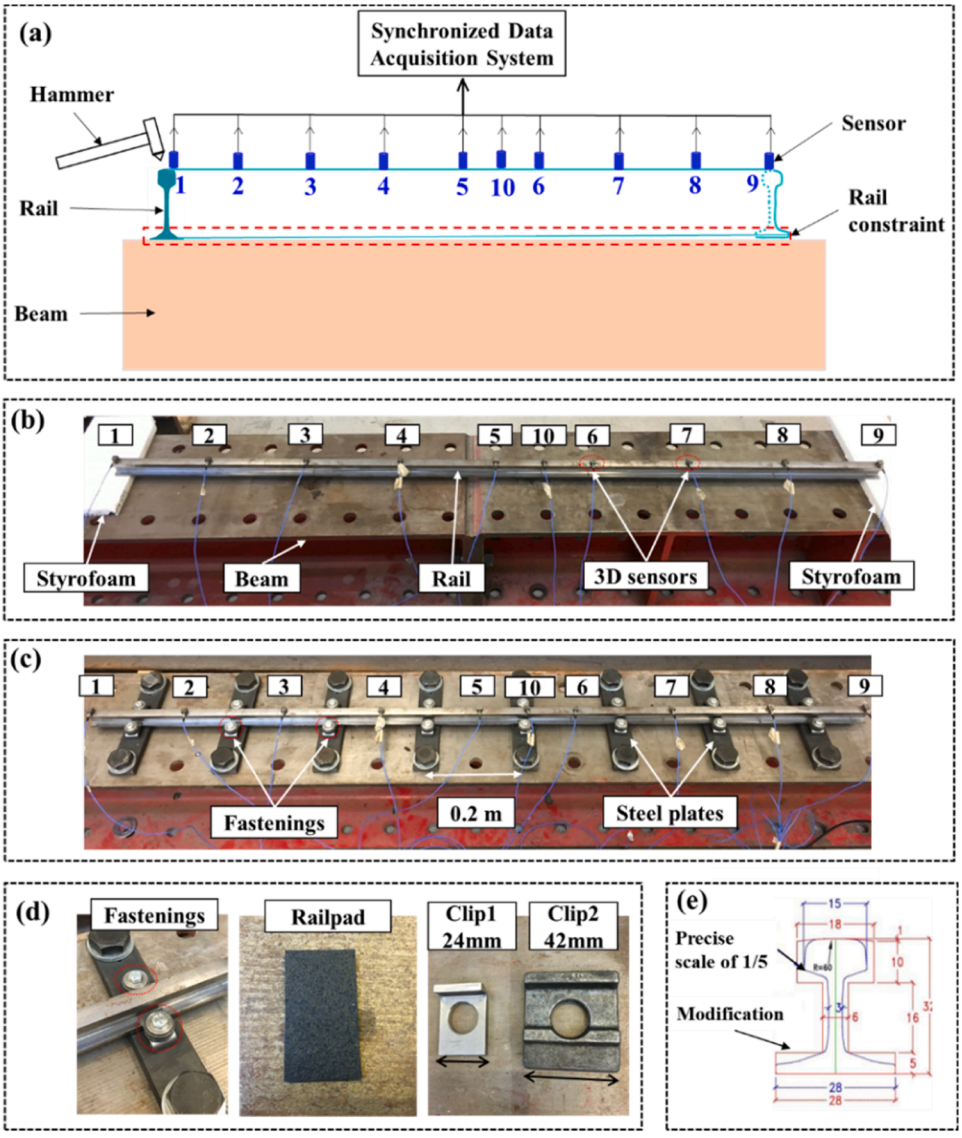

Fig. 4. Experimental setups for rail constraint design. (a) Schematic drawing; The experimental setup mainly consists of a scaled rail and a steel beam. The rail is supported on the beam by different types of rail constraints. A hammer test is performed to analyse the rail vibration characteristics by the ODS approach [62]. (b) setup for the free rail; the rail is supported on the beam by two soft styrofoam blocks at two ends. In this condition, the rail can be approximately considered to be in 'free vibrations'. (c) setup for the constrained rail; The rail is fixed on eight steel plates by different types of rail constraints. (d) fastenings consisting of the railpads and two types of clips; (e) scaled rail profile used on the setup.

Table 1
Five types of rail constraints in the experimental setups.

Types of rail constraints	Description	Purposes
1	Soft styrofoam blocks	To simulate the free boundary of the rail.
2	Railpads with half-tight clip1	To simulate the fastening constraint with insufficient toe loads.
3	Railpads with full-tight clip 1	To simulate the nominal fastening constraint.
4	Steel plates with full-tight clip 1	To simulate the relatively rigid rail constraint.
5	Steel plates with full-tight clip 2	To simulate the relatively rigid rail constraint.

in 'free vibrations'. For the second type (type 2), eight steel plates were rigidly fixed on the beam by bolts every 0.2 m, and the rail was constrained on the steel plates by eight fastenings, as shown in Fig. 4c and d. Each fastening consists of a railpad and a pair of clips (clip1 in Fig. 4d). The clip toe loads were applied through preload springs and the value was controllable by adjusting the spring compression displacement.

The preload spring consists of six conical disc springs in series with a combined stiffness of 180 N/mm. In this case (type 2), the toe load from each pair of clips was around 0.4 kN, which is equivalent to 10 kN of the full-scale rail, half the nominal value in the field track. This case was thus called half-tight clip1 to simulate the fastening constraint with insufficient toe load. For the third type (type 3), the clip load increased to 0.8 kN (called full-tight clip1) to simulate the nominal toe load of the fastening constraint in the field track. For the fourth type (type 4), the resilient railpads were removed and the rail was directly restricted on the steel plates by the full-tight clip1. In this condition, the rail was approximately regarded as 'rigidly' constrained on the steel beam. The last type (type 5) is the same as type 4, except that the narrower and thinner clip1 was replaced with the wider and thicker clip2, which was expected to provide a stronger constraint to the rail and more completely suppress the longitudinal compression modes. Overall, from type 1 to type 5, we designed to gradually strengthen the rail constraint to examine whether rail longitudinal compression modes can be effectively suppressed for corrugation mitigation.

A hammer test is performed to analyse the rail vibration characteristics by the ODS approach [62]. The sensor distribution of the hammer test in the setups is shown in Fig. 4a. In total, ten 3D accelerometers (PCB 356B21, denoted as 1–10 in Fig. 4a) were used. The first nine sensors were glued on the railhead surface with a spacing of 0.2 m. The tenth sensor was glued in the middle of sensor 5 and sensor 6. The responses of the ten accelerometers are denoted as follows,

$$a_i(t) = \left[a_{ix}(t),\ \ a_{iy}(t),\ \ a_{iz}(t)\right]^T, \quad i = 1, 2, ..., 10 \tag{4}$$

where $a_i(t)$ is the vector with the responses of the ith accelerometer, which includes three components a_{ix}(t), a_{iy} (t), a_{iz}(t) in the longitudinal, lateral, and vertical directions, respectively.

A small hammer (PCB 086C03) with a steel tip was used to excite the rail in the high-frequency range. The excitation positions were as close as possible to the sensor 1. Sensor 1 is at one of the free rail ends where the mode shapes have maximum deformation and thus the rail vibration modes can be excited with largest energy. Impacts were conducted in the longitudinal, lateral, and vertical directions, recorded as $F_{1x}(t)$, $F_{1y}(t)$, $F_{1z}(t)$. A synchronized data acquisition system recorded the excitation and the response signals. Five impacts in each direction were measured for each test with a sampling frequency of 51,200 Hz to reduce the random errors. The FRFs and corresponding ODSs can be obtained using Eqs. (2) and (3).

2.3.2. FE modelling of rail constraints

A 3D FE model of the rail-constraint system in Fig. 4 was developed, as shown in Fig. 5. The rail and the steel beam were modelled by 8-node solid elements with their nominal geometry and material. The cross-sections of the rail and the beam were discretized with an equal element edge length of 1.5 mm and 5 mm, respectively, as shown in Fig. 5b. The longitudinal element size of the rail was 5 mm, and that of the beam was 20 mm, as shown in Fig. 5c. The rail and beam material were treated as elastic isotropic with Young's modulus of 210 GPa, Poisson's ratio of 0.3, and density of 7850 kg/m^3. Free boundary conditions were applied to the two rail ends and the beam. The bottom nodes of the beams are fixed in three directions to simulate the foundation support.

The rail constraints of type 1, type 3 and type 5 in Table 1 were modelled by multiple spring-damper elements with various parameters and boundary conditions, as shown in Fig. 5d. One end of the spring-damper elements was connected to the rail bottom node (marked by R), and the other end to the beam node (marked by B). For type 1, a vanishingly small longitudinal stiffness of 0.3 kN/m of the spring-damper elements was used to simulate the styrofoam-block support. For type 3, the stiffness and damping of the spring-damper elements were identified by best fitting the simulations to the measurement results [77], which are 25 MN/m and 0.2 kNs/m, respectively. For type 5, the rail bottom nodes were fixed to simulate the rigid constraint.

2.4. Evaluation method of rail constraints for corrugation mitigation

Based on the modelling and identified parameters of rail constraints in Section 2.3, three rail constraint models (called type I, II, III) were built up and applied in the 3D FE vehicle-track interaction model (see Fig. 3) to examine their effects on corrugation mitigation, see a schematic drawing in Fig. 6. These three models in the vertical and lateral directions remained the same as the fastening model in Fig. 3c, while the rail longitudinal constraints were varied. In these models, rail longitudinal constraint was represented by multiple spring-damper elements as in Fig. 5d with various parameters and boundary conditions. Type I intends to simulate the longitudinal free boundary of the rail constraint type 1 in Table 1 with a small longitudinal stiffness of 1.5 kN/m equivalent to the parameters of type 1 by considering a scale factor of 1/5 [75]. Type II was built up to simulate the fastening longitudinal constraint of type 3 in Table 1 with the longitudinal stiffness and damping values of 125 MN/m and 5 kNs/m, respectively. The type III model fixed the rail bottom nodes above the sleeper in the longitudinal direction to simulate the rigid longitudinal constraint of type 5 in Table 1. The longitudinal wheel-rail dynamic contact force, which causes the differential wear and corrugation initiation (discussed in Section 3), will be evaluated with these three rail constraint models.

3. Corrugation reproduction and the initiation mechanism

With the initial excitation introduced by the fastening model in Fig. 3c, the longitudinal wheel-rail contact force (F_L) with strong fluctuation is induced, as shown in Fig. 7a. It has four main wavelength components in the range of 20–80 mm, which are 24.9 mm, 28.6 mm, 33.3 mm and 39.4 mm respectively, as shown in Fig. 7b. Amongst them, the wavelength of 28.6 mm has the highest PSD magnitude and is thus dominant. Fig. 7 also presents the calculated initial differential wear in the spatial and wavelength domains. Compared with F_L, it is found that initial differential wear and F_L have approximately the same trend and phase of the fluctuation amplitude in the spatial domain (see Fig. 7a) and four almost identical wavelength components (see Fig. 7b). It is hence concluded that longitudinal contact force F_L dominates initial differential wear. This initial differential wear causes corrugation initiation, and with the continuous accumulation of differential wear after multiple wheel passages, corrugation can consistently grow up to 80 μm [49]. Therefore, to mitigate or even eliminate corrugation, the fluctuation amplitude of the longitudinal contact force should be suppressed.

To better understand the fluctuation of the longitudinal contact force, its characteristic frequency f is calculated as follows.

$$f = v/\lambda \tag{5}$$

where v is the running speed 140 km/h, and λ is a characteristic wavelength, Corresponding to the four major wavelength components of

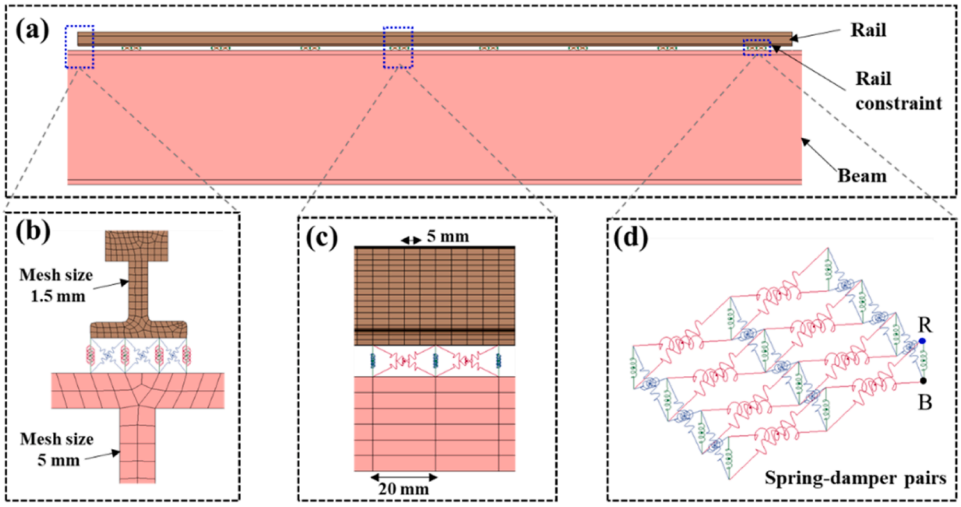

Fig. 5. 3D FE model of the rail-constraint system. (a) Front view; The rail and beam were modelled by 8-node solid elements, and rail constraint was modelled by multiple spring-damper elements. (b) cross-section mesh of the FE model; The element sizes of the rail and beam were 1.5 mm and 5 mm, respectively. (c) longitudinal mesh of the FE model; The longitudinal element size of the rail and the beam were 5 mm and 20 mm, respectively. (d) spring-damper elements of the rail constraint. 'R' designates the rail node of the spring-damper elements, and 'B' beam node.

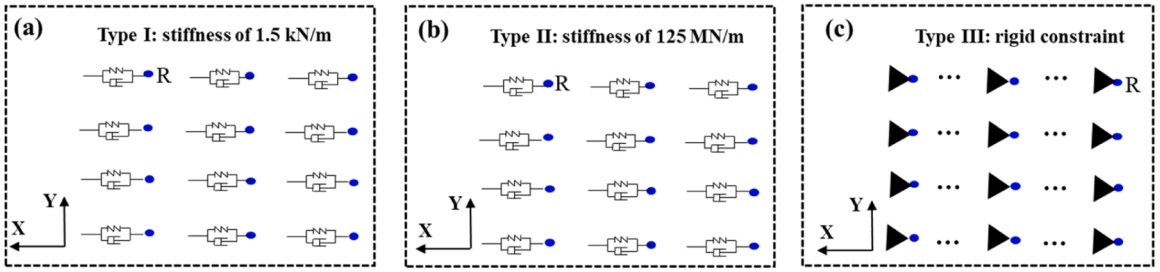

Fig. 6. Three rail constraint models in the FE vehicle-track interaction model. R' designates the constrained rail node. (a) Type I: rail constraint with a small longitudinal stiffness of 1.5 kN/m; (b) type II: rail constraint with the longitudinal stiffness and damping values of 125 MN/m and 5 kNs/m; (c) type III: rigid rail constraint in the longitudinal direction.

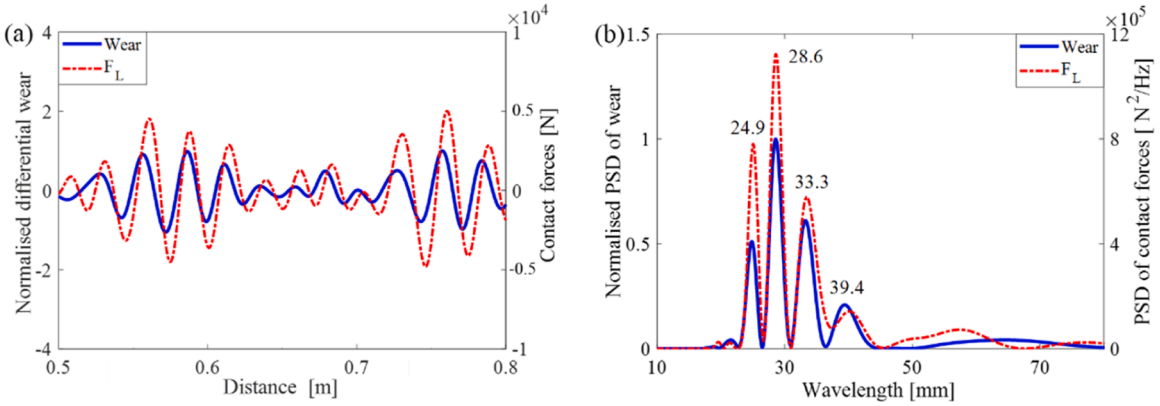

Fig. 7. The simulated longitudinal contact force and initial differential wear from the 3D FE vehicle-track interaction model (see Fig. 3) in spatial and wavelength domains. The results are band-pass filtered in the range of 20 – 80 mm. (a) Spatial domain; Initial differential wear and longitudinal contact force have approximately the same trend and phase of the fluctuation amplitude. (b) wavelength domain. Initial differential wear and longitudinal contact force have four almost identical wavelength components of 24.9 mm, 28.6 mm, 33.3 mm and 39.4 mm, respectively.

39.4 mm, 33.3 mm, 28.6 mm and 24.9 mm, the characteristic frequencies of the longitudinal contact force are calculated as 977 Hz, 1161 Hz, 1360 Hz and 1556 Hz, respectively, as shown in Fig. 8a and Table 2. These frequencies should be determined by the eigenmodes of the vehicle-track system. Fig. 8b shows the track longitudinal dynamics characterized by FRF at position 2 (see Fig. 3e). It is found from Fig. 8b

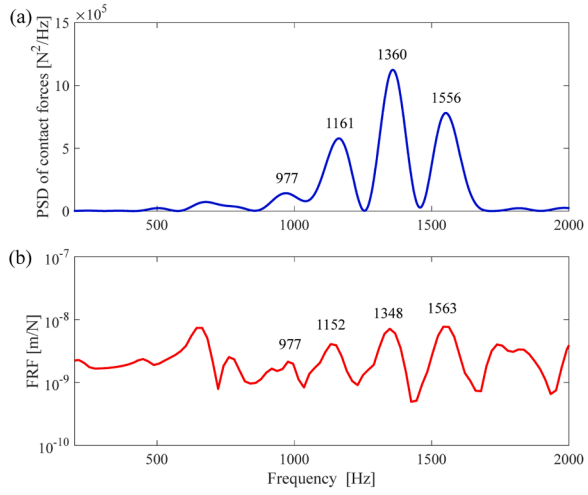

Fig. 8. Comparison of characteristic frequencies of the longitudinal contact force and the longitudinal FRF at position 2. (a) PSD of the longitudinal contact force; it has four characteristic frequencies of 977 Hz, 1161 Hz, 1360 Hz and 1556 Hz. (b) the longitudinal FRF at position 2. It has corresponding four peak frequencies of 977 Hz, 1152 Hz, 1338 Hz and 1563 Hz.

Table 2
Characteristic frequencies of the longitudinal contact force and longitudinal compression modes.

Longitudinal contact force frequency	977 Hz	1161 Hz	1360 Hz	1556 Hz
Longitudinal compression mode frequency with the fastening constraint in Fig. 3c	977 Hz	1152 Hz	1348 Hz	1563 Hz
Longitudinal compression mode frequency with fastening longitudinal stiffness of 100 MN/m	923 Hz	1172 Hz	1420 Hz	1671 Hz

and Table 2 that characteristic frequencies of the longitudinal force correspond well to the peak frequencies of the FRF, indicating that rail vibration modes related to these peaks induce the fluctuation of longitudinal contact force and dominate the corrugation initiation. In order to identify these modes, the corresponding ODSs at these peak frequencies were derived and compared with rail longitudinal compression modes from modal analysis, as shown in Fig. 9. The colour contrast in the mode shapes indicates the relative deformations of the elements. Blue is the minimum deformation, and red is the maximum. It can be seen from Fig. 9 that the ODSs at 977 Hz, 1161 Hz, 1360 Hz and 1556 Hz are consistent with the deformations of rail longitudinal compression modes at 923 Hz, 1172 Hz, 1420 Hz and 1671 Hz, respectively, indicating that the peaks in Fig. 8b correspond to longitudinal compression modes. It should be noted that the fastening longitudinal rigid constraint in Fig. 3c was replaced by the approximately equivalent longitudinal springs with a stiffness of 100 MN/m for the modal analysis. It is thus inferred that the longitudinal compression modes are responsible for the corrugation initiation.

Based on the results of Figs. 7, 8 and 9, the corrugation initiation

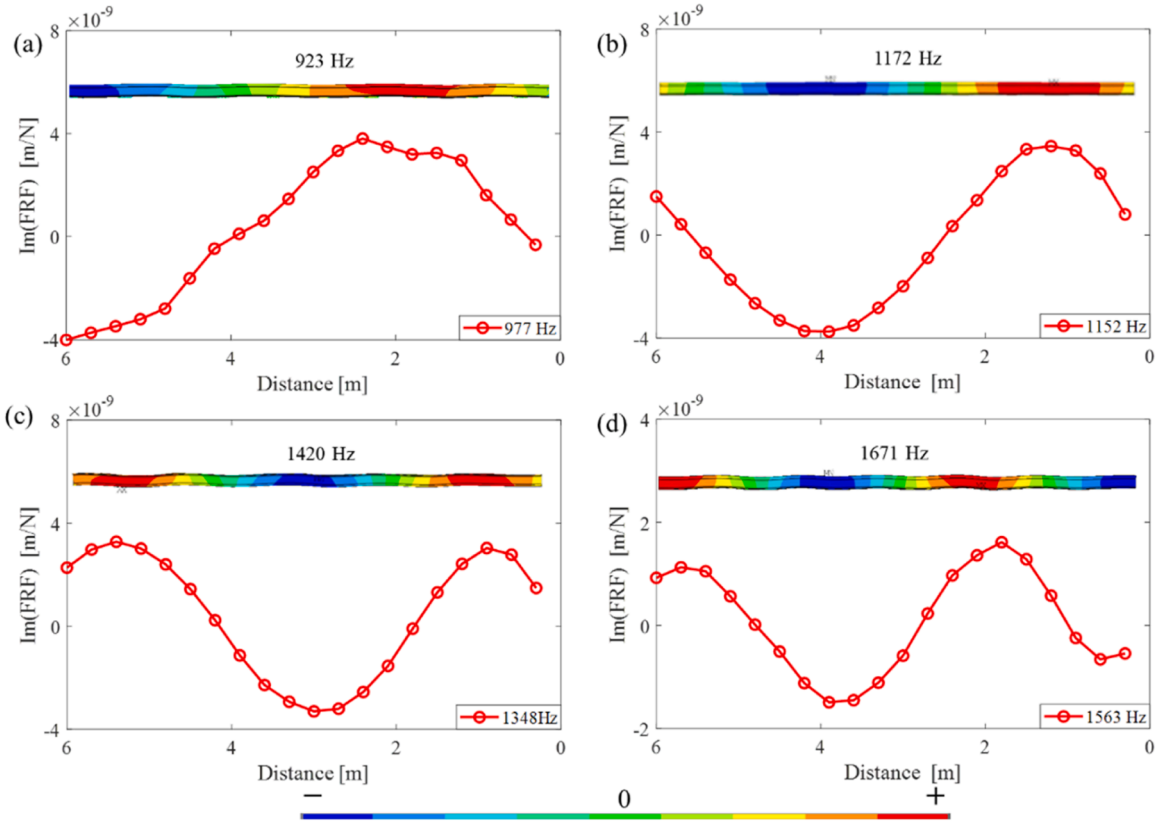

Fig. 9. Comparison of ODSs at the four peak frequencies of the longitudinal FRF and rail longitudinal compression modes. (a) ODS at 977 Hz and longitudinal compression mode at 923 Hz; (b) ODS at 1152 Hz and longitudinal compression mode at 1172 Hz; (c) ODS at 1348 Hz and longitudinal compression mode at 1420 Hz; ODS at 1563 Hz and longitudinal compression mode at 1671 Hz. The colour contrast in the mode shapes indicates the relative deformations of the elements. Blue is the minimum deformation, and red is the maximum.

mechanism is further understood. With the fastening constraint in Fig. 3c, rail longitudinal compression modes are released, as shown in Fig. 8b. When the wheel rolls over the rail, some of them are excited, and induce the fluctuation of the longitudinal wheel-rail contact force with the corresponding frequencies, resulting in initial differential wear and corrugation. Based on this insight, an approach to mitigate or even eliminate corrugation is proposed. That is to design a new rail constraint that can effectively suppress rail longitudinal compression modes so that longitudinal contact force fluctuates little, differential wear can barely accumulate, and corrugation can hardly initiate.

4. Experimental results and modelling of rail constraints for corrugation mitigation

In this section, the influences of five types of rail constraints (see Table 1) on rail vibration modes, especially longitudinal compression modes, are analysed. Rail constraints type 1, type 3 and type 5 in Table 1 are modelled and validated against the measurement results.

4.1. Experimental results and discussion

In this subsection, the experimental results of free rail vibrations (Section 4.1.1), rail vibrations under fastening constraints (Section 4.1.2) and rigid rail constraints (Section 4.1.3) are present. These results are further discussed in Section 4.1.4.

4.1.1. Free rail vibrations

Fig. 10 shows the FRFs with the rail constraint type 1 at accelerometer 1 in the vertical, longitudinal, and lateral directions up to 10 kHz. The rail with this constraint can be approximately considered to be

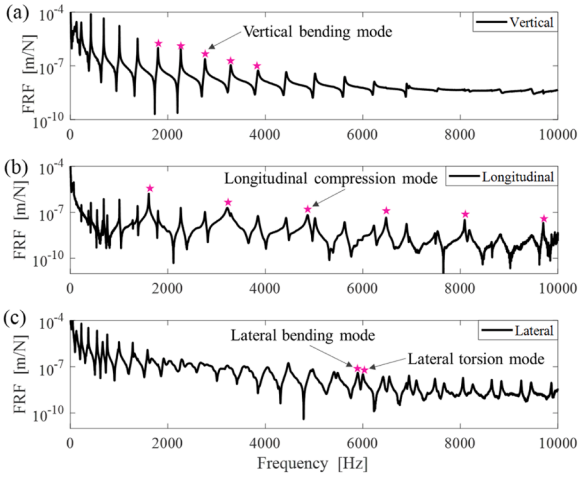

Fig. 10. FRFs with the rail constraint type 1 at accelerometer 1 in the (a) vertical, (b) longitudinal and (c) lateral directions. In this figure, (★) show some examples of vertical bending modes, longitudinal compression modes, lateral bending and torsion modes.

in 'free vibrations', as described in Fig. 4b and Table 1. The set of major peaks in the vertical FRF (★ in Fig. 11a) correspond to the rail vertical bending modes, and those in the longitudinal FRF (★ in Fig. 11b) correspond to longitudinal compression modes. Two sets of major peaks in the lateral FRF are coupled together (★ in Fig. 11c), representing lateral bending and lateral torsion modes, respectively

Based on the FRF measurement results, the wavenumber-frequency

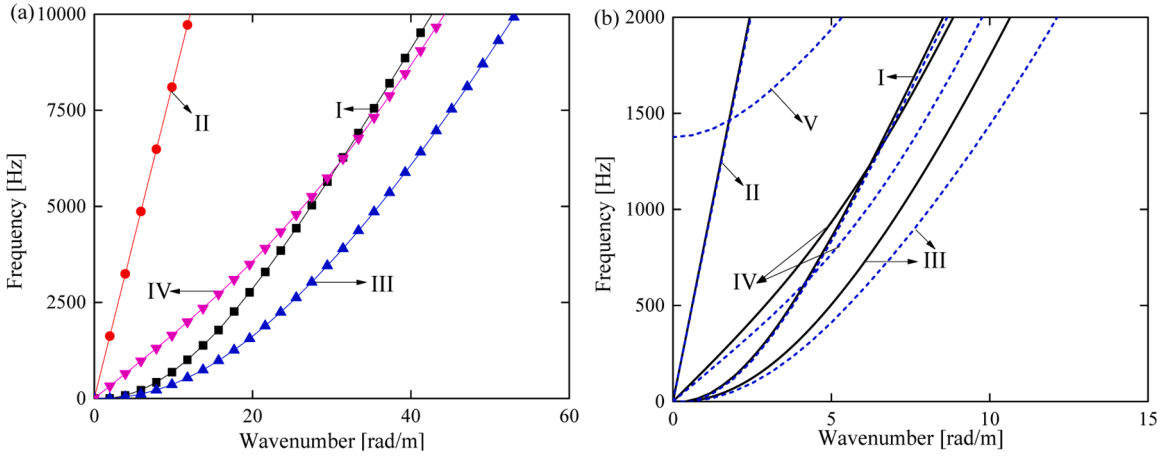

Fig. 11. Wavenumber-frequency dispersion curves of the 1/5 scaled and full-scale free rails. (a) 1/5 scaled rail; (b) comparison between 1/5 scaled rail (—after modification) and full-scale rail (—). The result of the full-scale rail is from [62]. In this figure, 'I' refers to vertical bending waves, 'II' longitudinal compression waves, 'III' lateral bending waves, 'IV 'lateral torsion waves, 'V' web 1st bending waves.

dispersion curves of the 1/5 scaled rail were derived by connecting the discrete wavenumber-frequency points, as shown in Fig. 11a. The natural frequencies were derived from the major peak frequencies of FRFs in Fig. 10, and the corresponding wavenumbers are estimated with $k = N\pi/L$, where λ is the wavelength, k is the wavenumber, N is an integer, and L is the rail length. Four types of waves, vertical bending waves (I), longitudinal compression waves (II), lateral bending waves (III) and lateral torsion waves (IV), were identified. Fig. 11b compares the dispersion curves of the 1/5 scaled rail with those of full-scale rail. It should be noted that the frequency and wavenumber of the scaled rail have been modified by a scaling factor of 1/5 for comparison based on the similarity law [75]. It can be seen that the dispersion curves of longitudinal compression waves (II) overlap almost completely with each other in these two cases. Differences were observed for vertical bending waves (I) above 1500 Hz, where significant cross-section deformations start to occur [62]. The dispersion curves of two lateral waves of the 1/5 scaled rail are considerably different from those of full-scale rail. The difference in these two cases is caused by the modification of the scaled rail profile, as shown in Fig. 4e, which influences the rail vibration modes involving cross-section deformation. This also explains the absence of the web 1st bending waves (V) of the scaled rail in Fig. 11b, whose cut-on frequency is beyond 2000 Hz because of the wider rail web, compared to the precisely 1/5 scaled one.

In summary, longitudinal compression modes/waves of the scaled rail are equivalent to those of full-scale rail, which provides a basis for rail constraint design on the scaled rail instead of the full-scale rail. Despite the slight deviation, the vertical bending modes/waves of the scaled rail can be approximately regarded as the same as those of the full-scale rail. However, the lateral modes/waves show a significant difference in these two cases because of the imperfectly scaled rail profile.

4.1.2. *Rail vibrations under fastening constraints*

Fig. 12 shows the FRFs with rail constraints type 1, 2 and 3 at accelerometer 1 in the vertical, longitudinal, and lateral directions up to 10 kHz. Type 2 and type 3 correspond to railpads with half-tight and full-tight clip 1, respectively, as listed in Table 1, which are used to simulate field fastening constraints. Compared to type 1, vertical bending modes with type 2 and type 3 were significantly suppressed and could barely be distinguished in the vertical FRFs, as shown in Fig. 12a. Only one dominant peak was observed at around 1050 Hz, corresponding to the rail resonance mode on the fastening vertical stiffness. The tightness (half- or full-tight) of clip 1 has an insignificant influence on the vertical FRFs. Different from the vertical bending modes, the longitudinal compression modes were still identifiable under the fastening

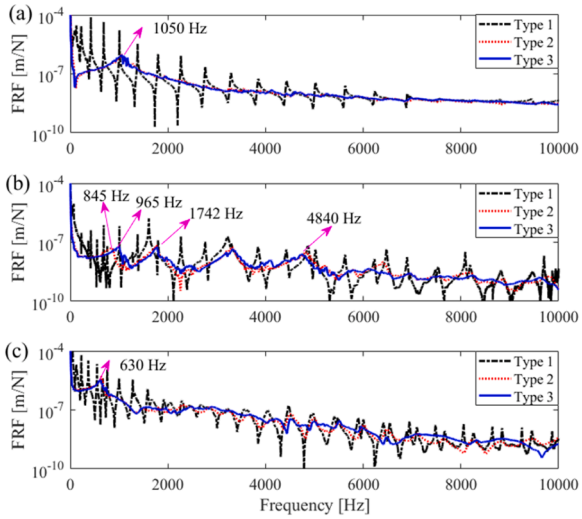

Fig. 12. FRFs with rail constraints type 1, 2 and 3 at accelerometer 1 in the (a) vertical, (b) longitudinal and (c) lateral directions. The pink arrow in (a) shows the vertical resonance mode at 1050 Hz, the arrows in (b) indicate the longitudinal resonance modes at 845 Hz for type 2 and 965 Hz for type 3, and the arrow in (c) shows the lateral resonance mode at 630 Hz.

constraint, although their fluctuation amplitudes were considerably reduced. When the tightness of clip 1 increased from type 2 to type 3, the overall fluctuation amplitudes of longitudinal compression modes became slightly smaller, and the rail longitudinal resonance mode was shifted from about 845 Hz to 965 Hz. Fig. 13 shows that the ODSs of type 3 at 1742 Hz and 4840 Hz have shapes similar to the ODSs of type 1 at 1610 Hz and 4870 Hz and are consistent with the deformations of longitudinal compression modes of the free rail at 1620 Hz and 4880 Hz. This result confirms that the major peaks in Figs. 11b and 12b correspond to longitudinal compression modes, which share features similar to those of the full-scale rail in Fig. 9. Similar to vertical bending modes, rail lateral bending and torsion modes were also significantly suppressed by the fastening constraint with half-tight clip 1, and became almost invisible from the lateral FRF with full-tight clip 1, as shown in Fig. 12c.

Overall, vertical bending modes and lateral bending and torsion modes are effectively suppressed by the fastening constraint with full-tight clip 1, while longitudinal compression modes still have relatively strong fluctuation amplitude. This result agrees with the findings in [62] that, the fastenings constrain the longitudinal rail vibrations less

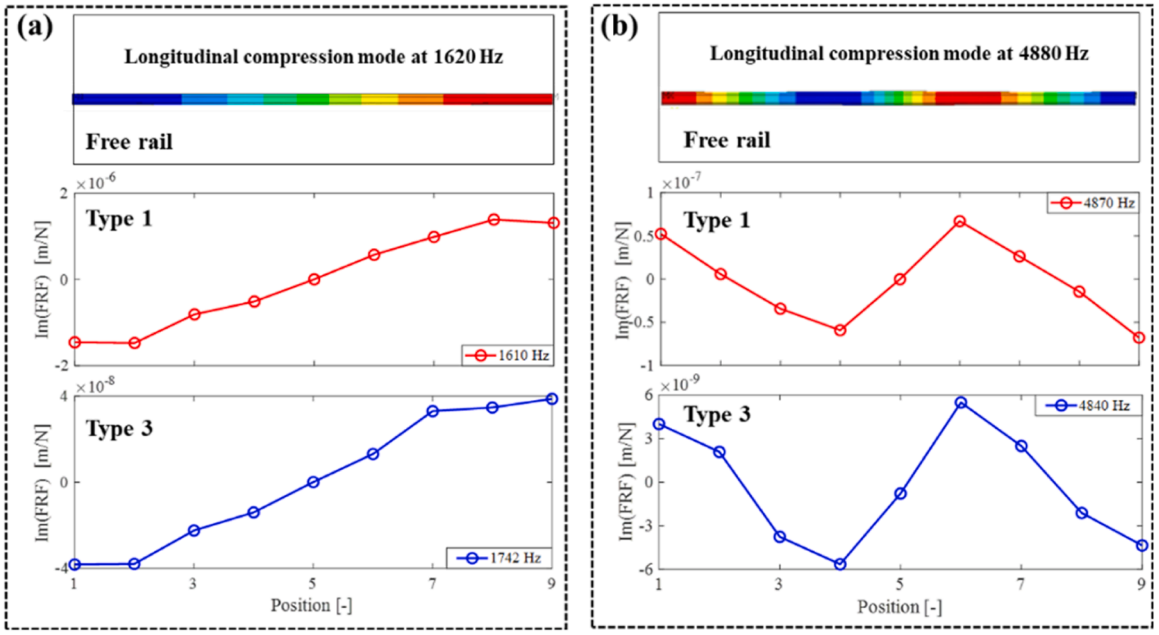

Fig. 13. Comparison of longitudinal ODSs with rail constraints type 1 and type 3 and longitudinal compression modes of free rail. (a) Comparison of ODS with type 1 at 1610 Hz, ODS with type 3 at 1742 Hz, and longitudinal compression mode at 1620 Hz; (b) comparison of ODS with type 1 at 4870 Hz, ODS with type 3 at 4840 Hz and longitudinal compression mode at 4880 Hz.

strongly compared to the vertical and lateral directions.

4.1.3. *Rail vibrations under rigid rail constraints*

Fig. 14 shows the FRFs with rail constraints types 3, 4 and 5 at accelerometer 1 in the vertical, longitudinal, and lateral directions. Type 4 and type 5 correspond to steel plates with full-tight clip 1 and clip 2, respectively, as listed in Table 1, which are used to simulate relatively rigid rail constraints. Compared to clip 1, clip 2 is wider and thicker, which is expected to provide a stronger constraint to the rail and more completely suppress the longitudinal compression modes. It can be seen from Fig. 14a and c that the vertical bending modes and lateral bending and torsion modes are effectively suppressed by the two types of rigid rail constraints. Despite the significant mitigation, longitudinal compression modes are still identifiable at about 4935 Hz and 6230 Hz (indicated by pink arrows in Fig. 14b) with type 4. By replacing clip 1 with clip 2, longitudinal compression modes are almost invisible in the longitudinal FRF, indicating the type 5 is capable of completely suppressing them. In addition, compared to type 3, the rail resonance modes in the vertical, longitudinal and lateral directions have been shifted to 1500 Hz, 1495 Hz and 1025 Hz, respectively, with reduced amplitude, as shown in Fig. 14. That is because the support stiffness of steel pads of type 4 and 5 are larger than the resilient railpads of type 3.

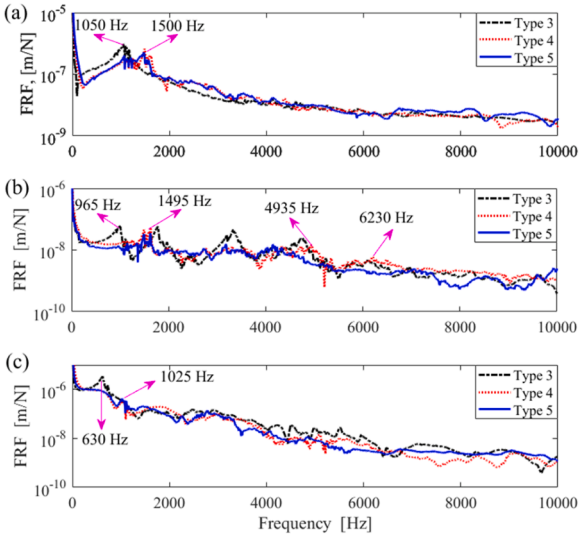

Fig. 14. FRFs with rail constraints types 3, 4 and 5 at accelerometer 1 in the (a) vertical, (b) longitudinal and (c) lateral directions. The pink arrows in (a) show the vertical resonance mode shifts from 1050 Hz with type 3 to 1500 Hz with type 5, arrows in (b) show the longitudinal resonance mode shifts from 965 Hz with type 3 to 1495 Hz with type 5, and arrows in (c) show the lateral resonance mode shifts from 630 Hz with type 3 to 1025 Hz with type 5.

4.1.4. *Discussion of experimental results*

In this work, five types of rail constraints were designed and their influences on rail vibration modes were analysed. Overall, these five types of rail constraints can be characterized into three categories, 'zero stiffness' of free rail (type 1), 'finite stiffness' of fastening constraint (type 2 and 3), 'infinite stiffness' of rigid constraint (type 4 and 5). More specifically, the parameters (i.e., stiffness and damping) of the nominal fastening constraint (type 3) are 120 MN/m and 2 kNs/m vertically, 25 MN/m and 0.2 kNs/m longitudinally, and 37 MN/m and 0.8 kNs/m laterally. Those of free rail and rigid rail constraint are considered as zero and infinite, respectively.The experimental results indicate that longitudinal compression modes/waves of the scaled free rail are equivalent to those of full-scale rail within 2 kHz with a scaling factor of 1/5. That is because the dispersion relation of longitudinal waves of free rail is only determined by the rail material, i.e., young's modulus and density. However, the rail vibration modes involving cross-section deformation, such as lateral torsion modes, web 1st bending modes, are significantly influenced by the imperfectly scaled rail profile. The fastening constraint with finite stiffness (type 3) can effectively suppress vertical bending modes and lateral modes with appropriate parameter design, but cannot completely restrict longitudinal compression modes. Therefore, we further strengthened the rail constraints with 'infinite stiffness' (type 5). Experimental results indicated this constraint can effectively suppress longitudinal compression modes and thus be supposed to mitigate or even eliminate corrugation.

4.2. Validation of FE modelling of rail constraints

Fig. 15 shows the simulated and measured longitudinal FRFs with rail constraints type 1, type 3 and type 5 to consider the cases of 'zero stiffness', 'finite stiffness' and 'infinite stiffness', respectively. The overall tendencies and fluctuation amplitude from the simulations match the measurements well. The simulations identify almost all the peaks in the measured FRFs, as shown in Fig. 16a and b. In these three cases, it is observed that the simulations seem to overestimate the FRFs at higher frequencies above 7 kHz. The reason is that the excitation energy of the small hammer in the test has considerably dropped over 7 kHz [67] and thus the rail-constraint system cannot be sufficiently excited at higher frequencies, leading to the smaller FRFs of the measurements. Overall, good agreement has been achieved between the simulations and the measurements, indicating the modelling of the rail constraints can accurately reproduce the dynamic behaviours of the rail-constraint system.

5. Evaluation results of rail constraints for corrugation mitigation

Three rail constraint models (type I, II, III in Fig. 6) were applied in the 3D FE vehicle-track interaction model to examine their effectiveness on corrugation mitigation. Fig. 16 shows the longitudinal wheel-rail contact forces with these constraint models. It can be seen that the fluctuation amplitude of longitudinal contact force with type III is significantly smaller than those with type I and II. Therefore the resulting initial differential wear is much smaller, and corrugation can hardly initiate. This result indicates the rail constraint model type III, corresponding to the rigid constraint of type 5 in the experimental setup (see Table 1), can effectively suppress rail longitudinal compression mode, reduce the fluctuation of longitudinal contact force, and mitigate corrugation.

In addition, it is observed that type II considerably reduces the fluctuation amplitude of longitudinal force, compared to that of type I. Fig. 16b also shows that the major frequency components (marked by ▼ and number) of longitudinal force with types I and II are different from each other. That is because of the different fastening parameters in these two cases, which influence the eigen frequencies of the vehicle-track system and thus characteristic frequencies of longitudinal force and corrugation. To gain insight into the dynamic behaviour of the vehicle-track system with type I and type II, a modal analysis was performed and their longitudinal compression modes were compared in Fig. 17 and Table 3. It is found that characteristic frequencies of the longitudinal force correspond well to the eigen frequencies of longitudinal compression modes, confirming that longitudinal compression modes are responsible for corrugation initiation. Besides, the mode frequencies with type I are shifted to larger values with type II because of the larger fastening longitudinal stiffness.

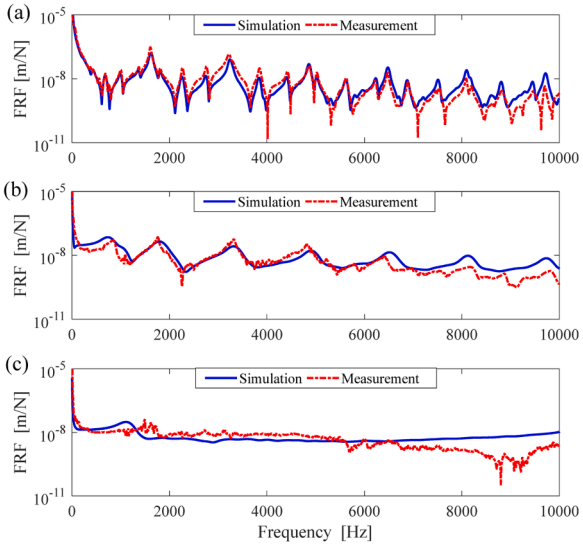

Fig. 15. Validation of longitudinal FRFs with rail constraints type 1, type 3 and type 5. (a) Type 1, free rail; (b) type 3, rail under the fastening constraint; (c) type 5, rail under the rigid constraint.

6. Discussions

In this paper, we employ a 3D FE vehicle-track interaction model with degraded fastenings and successfully reproduced rail corrugation. Further ODS analysis indicates rail longitudinal compression modes and the induced longitudinal dynamic contact force are dominant for corrugation initiation. Therefore, a new rail constraint is subsequently designed that can effectively suppress rail longitudinal modes, fluctuation of longitudinal contact force, and corrugation initiation. This paper first points out a direction for field corrugation mitigation by strengthening the rail longitudinal constraint. It should be noted that this new rail constraint is still a concept design in the current stage and needs to be further experimentally verified [75]. Its manufacturing and installation cost also needs to be considered compared to those of the current fastenings and the preventive rail grinding for corrugation control before the final application to the field.

Corrugation formation process can be divided into two stages, i.e., initiation and growth. This work aims at mitigating corrugation in the initiation stage and thus focuses on investigating the longitudinal dynamics of the vehicle-track system which dominates corrugation initiation. In our parallel paper, corrugation formation mechanism including both the initiation and growth is analysed in detail and it is found vertical dynamics of vehicle-track system play an important role in the corrugation growth stage. Since corrugation in this paper refers to short pitch corrugation mainly occurring on straight or gentle tracks, the lateral vehicle-track dynamic interaction is considered as secondary to corrugation formation and hence not analysed in this work. Future research can readily include it with the current 3D FE model [67,78].

In this work, the vehicle-track system is simplified by a single wheel-track dynamic interaction model. In the literature, some researchers have shown that rail vibrational wave interference amongst multiple wheels and the wheelset structural flexibility are both important for corrugation development [27,28,79]. The multiple wheels or wheelsets could be very important but might not be the only condition to determine corrugation formation, otherwise rail corrugation will occur everywhere on the track. Besides, both the FE simulation in this paper and laboratory tests using the V-Track test rig [75,76] show that the single wheel-track system can successfully reproduce corrugation. Future work will be performed to further study the influence of multiple wheels and wheelsets on corrugation formation. In addition, the current FE model simulates vehicle-track interaction and corrugation on a straight track, and it is also possible to simulate rail corrugation on the curved tracks with small radii [80] with certain modifications.

7. Conclusions

This paper proposes a methodology to mitigate short pitch corrugation by rail constraint design. This methodology includes four steps. In Step 1, short pitch corrugation were numerically reproduced by employing a 3D FE vehicle-track interaction model with degraded fastenings. In Step 2, the corrugation initiation mechanism was identified by comparing the ODSs with rail longitudinal compression modes. In Step 3, five types of rail constraints were designed and their influences on rail vibration modes were analysed. Models of rail constraints types 1, 3 and 5 were built up and validated. In Step 4, the rail constraint models from Step 3 were applied in the FE vehicle-track interaction model, and their effectiveness on corrugation mitigation was evaluated.

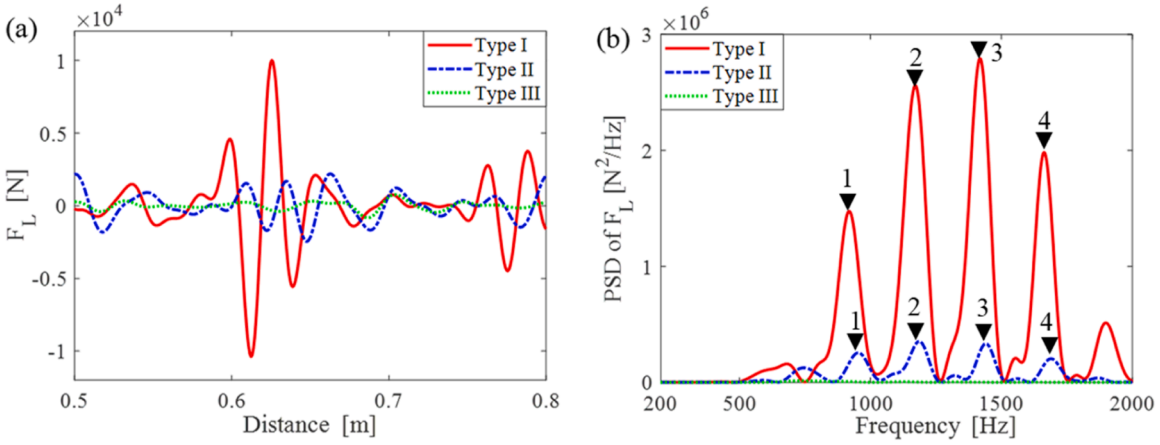

Fig.16. Longitudinal wheel-rail contact forces with rail constraint models type I, II, III in the spatial and frequency domains. (a) Spatial domain; The fluctuation amplitude of longitudinal contact force with type III is significantly smaller than those with type I and II. (b) frequency domain. The marks (▼) indicate the characteristic frequencies of the contact forces with type I and type II.

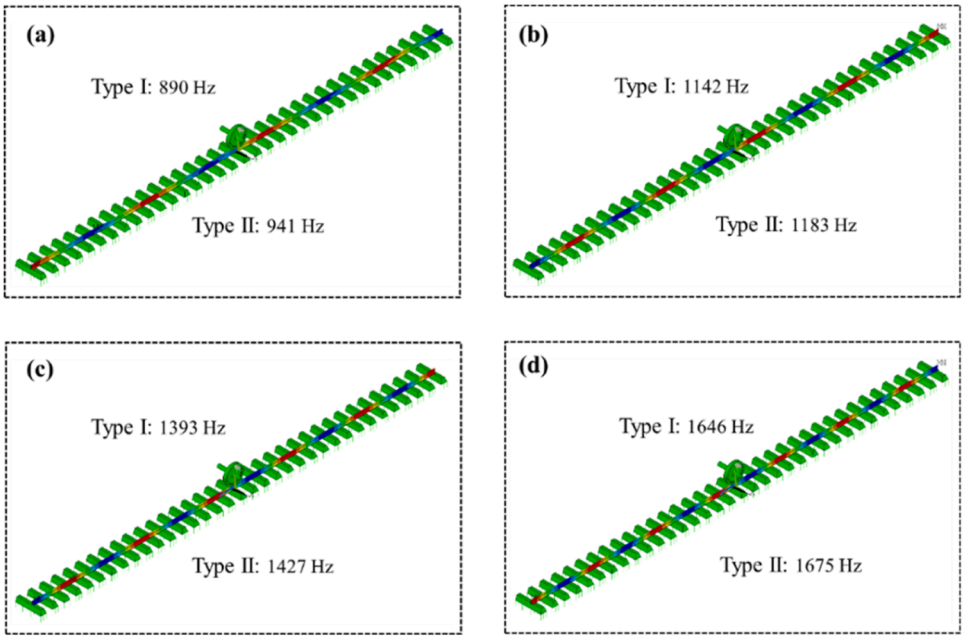

Fig. 17. Rail longitudinal compression modes with rail constraint models type I and II. (a) 890 Hz for type I and 941 Hz for type II with the same mode shape; (b) 1142 Hz for type I and 1183 Hz for type II; (c) 1393 Hz for type I and 1427 Hz for type II; (d) 1646 Hz for type I and 1675 Hz for type II.

Table 3
Comparison of characteristic frequencies of longitudinal force and longitudinal compression modes with rail constraint models type I and type II.

Number in Fig. 16b	Longitudinal force peak frequency with type I in Fig. 16b	Mode frequency with type I in Fig. 17	Longitudinal force peak frequency with type II in Fig. 16b	Mode frequency with type II in Fig. 17
1	915 Hz	890 Hz	958 Hz	941 Hz
2	1170 Hz	1142 Hz	1184 Hz	1183 Hz
3	1418 Hz	1393 Hz	1440 Hz	1427 Hz
4	1663 Hz	1646 Hz	1691 Hz	1675 Hz

The main findings are summarized as follows.

The corrugation initiation mechanism is identified from the analysis of ODSs. With a particular fastening constraint, rail longitudinal compression modes may not be effectively suppressed. When the wheel rolls over the rail, some of them are excited, and induce longitudinal wheel-rail dynamic contact force with corresponding frequencies, resulting in the initial differential wear and corrugation. Based on this corrugation initiation mechanism, an approach is proposed to mitigate or even eliminate corrugation. That is to design a new rail constraint that can effectively suppress rail longitudinal compression modes so that the induced longitudinal contact force fluctuates little, differential wear can barely accumulate, and corrugation can hardly initiate.

Five type of rail constraints are designed and evaluated, and amongst them, a relatively rigid constraint (type 5) can completely suppress rail longitudinal compression modes. Afterwards, this rail constraint model is applied in the FE vehicle-track model and the simulated longitudinal contact force has a significantly small fluctuation amplitude so that corrugation can hardly initiate. Besides, it is found that fastening longitudinal parameters influence the frequencies of longitudinal compression modes and thus the characteristic wavelengths/frequencies and spatial distribution of short pitch corrugation.

Overall, this paper first points out a direction for short pitch

corrugation mitigation in the field by strengthening the rail longitudinal constraint. In future work, we will perform the experimental validation of corrugation initiation mechanism and the designed new rail constraint for corrugation mitigation by employing an innovative V-Track test rig.

CRediT authorship contribution statement

Pan Zhang: Conceptualization, Methodology, Formal analysis, Data curation, Investigation, Software, Writing – original draft, Writing – review & editing. **Shaoguang Li:** Data curation, Investigation, Software, Writing – review & editing. **Zili Li:** Conceptualization, Methodology, Investigation, Resources, Writing – review & editing, Supervision, Project administration, Funding acquisition.

Declaration of Competing Interest

The authors declare that they have no known competing financial interests or personal relationships that could have appeared to influence the work reported in this paper.

Data Availability

Data will be made available on request.

Acknowledgments

The first author thanks the China Scholarship Council for the support.

References

[1] Grassie S, Kalousek J. Rail corrugation: characteristics, causes and treatments. Proc Inst Mech Eng Part F J Rail Rapid Transit 1993;207:57–68.
[2] Grassie S. Rail corrugation: characteristics, causes, and treatments. Proc Inst Mech Eng Part F J Rail Rapid Transit 2009;223:581–96.
[3] Li Z, Dollevoet R, Molodova M, Zhao X. Squat growth – some observations and the validation of numerical predictions. Wear 2011;271:148–57.
[4] Li S, Li Z, Núñez A, Dollevoet R. New insights into the short pitch corrugation enigma based on 3D-FE coupled dynamic vehicle-track modeling of frictional rolling contact. Appl Sci 2017;7:807.
[5] Xu J, Wang K, Liang X, Gao Y, Liu Z, Chen R, Wang P, Xu F, Wei K. Influence of viscoelastic mechanical properties of rail pads on wheel and corrugated rail rolling contact at high speeds. Tribol Int 2020;151:106523.
[6] Sadeghi J, Hasheminezhad A. Correlation between rolling noise generation and rail roughness of tangent tracks and curves in time and frequency domains. Appl Acoust 2016;107:10–8.
[7] Han J, Xiao X, Wu Y, Wen Z, Zhao G. Effect of rail corrugation on metro interior noise and its control. Appl Acoust 2018;130:63–70.
[8] Xin T, Wang S, Gao L, Huo H, Ding Y, Wang P, Chen P, Liu P. Field measurement of rail corrugation influence on environmental noise and vibration: a case study in China. Measurement 2020;164:108084.
[9] Clark R, Dean P, Elkins J, Newton S. An investigation into the dynamic effects of railway vehicles running on corrugated rails. J Mech Eng Sci 1982;24:65–76.
[10] Deng X, Qian Z, Li Z, Dollevoet R. Investigation of the formation of corrugation-induced rail squats based on extensive field monitoring. Int J Fatigue 2018;112:94–105.
[11] Grassie S, Saxon M, Smith J. Measurement of longitudinal rail irregularities and criteria for acceptable grinding. J Sound Vib 1999;227:949–64.
[12] Cuervo P, Santa J, Toro A. Correlations between wear mechanisms and rail grinding operations in a commercial railroad. Tribol Int 2015;82:265–73.
[13] Liu YM, Yang TY, He Z, Li JY. Analytical modeling of grinding process in rail profile correction considering grinding pattern. Arch Civil Mech Eng 2018;18:669–78.
[14] Sun Y, Wang P, Lu J, Xu J, Wang P, Xie S, Li Y, Dai J, Wang B, Gao M. Rail corrugation inspection by a self-contained triple-repellent electromagnetic energy harvesting system. Appl Energy 2021;286:116512.
[15] Wei Z, Sun X, Yang F, Ke Z, Lu T, Zhang P, Shen C. Carriage interior noise-based inspection for rail corrugation on high-speed railway track. Appl Acoust 2022;196:108881.
[16] Xie Q, Tao G, He B, Wen Z. Rail corrugation detection using one-dimensional convolution neural network and data-driven method. Measurement 2022:111624.
[17] Meehan P, Bellette P, Batten R, Daniel W, Horwood R. A case study of wear-type rail corrugation prediction and control using speed variation. J Sound Vib 2009;325:85–105.
[18] Bellette P, Meehan P, Daniel W. Contact induced wear filtering and its influence on corrugation growth. Wear 2010;268:1320–8.
[19] Vuong T, Meehan P, Eadie D, Oldknow K, Elvidge D, Bellette P, Daniel W. Investigation of a transitional wear model for wear and wear-type rail corrugation prediction. Wear 2011;271:287–98.
[20] Correa N, Vadillo E, Santamaria J, Herreros J. A versatile method in the space domain to study short-wave rail undulatory wear caused by rail surface defects. Wear 2016;352:196–208.
[21] Santa J, Toro A, Lewis R. Correlations between rail wear rates and operating conditions in a commercial railroad. Tribol Int 2016;95:5–12.
[22] Zhao X, Zhang P, Wen Z. On the coupling of the vertical, lateral and longitudinal wheel-rail interactions at high frequencies and the resulting irregular wear. Wear 2019;430:317–26.
[23] Hempelmann K, Knothe K. An extended linear model for the prediction of short pitch corrugation. Wear 1996;191:161–9.
[24] Muller S. A linear wheel–track model to predict instability and short pitch corrugation. J Sound Vib 1999;227:899–913.
[25] Afferrante L, Ciavarella M. Short-pitch rail corrugation: a possible resonance-free regime as a step forward to explain the "enigma"? Wear 2009;266:934–44.
[26] Johansson A, Nielsen JC. Rail corrugation growth—Influence of powered wheelsets with wheel tread irregularities. Wear 2007;262:1296–307.
[27] Wu T, Thompson D. An investigation into rail corrugation due to micro-slip under multiple wheel/rail interactions. Wear 2005;258:1115–25.
[28] Ma C, Gao L, Xin T, Cai X, Nadakatti MM, Wang P. The dynamic resonance under multiple flexible wheelset-rail interactions and its influence on rail corrugation for high-speed railway. J Sound Vib 2021;498:115968.
[29] Batten R, Bellette P, Meehan P, Horwood R, Daniel W. Field and theoretical investigation of the mechanism of corrugation wavelength fixation under speed variation. Wear 2011;271:278–86.
[30] Bellette P, Meehan P, Daniel W. Validation of a tangent track corrugation model with a two disk test rig. Wear 2011;271:268–77.
[31] Meehan P, Batten R, Bellette P. The effect of non-uniform train speed distribution on rail corrugation growth in curves/corners. Wear 2016;366:27–37.
[32] Chen G, Zhou Z, Ouyang HJ, Jin X, Zhu M, Liu Q. A finite element study on rail corrugation based on saturated creep force-induced self-excited vibration of a wheelset–track system. J Sound Vib 2010;329:4643–55.
[33] Cui X, Chen G, Zhao J, Yan W, Ouyang H, Zhu M. Field investigation and numerical study of the rail corrugation caused by frictional self-excited vibration. Wear 2017;376:1919–29.
[34] Li W, Zhou Z, Zhao X, Wen Z, Jin X. Formation mechanism of short-pitch rail corrugation on metro tangent tracks with resilient fasteners. Veh Syst Dyn 2022:1–24.
[35] Escalona JL, Aceituno JF. Multibody simulation of railway vehicles with contact lookup tables. Int J Mech Sci 2019;155:571–82.
[36] Yu X, Aceituno JF, Kurvinen E, Matikainen MK, Korkealaakso P, Rouvinen A, Jiang D, Escalona JL, Mikkola A. Comparison of numerical and computational aspects between two constraint-based contact methods in the description of wheel/rail contacts. Multibody Syst Dyn 2022;54:303–44.
[37] Shen C, Deng X, Wei Z, Dollevoet R, Zoeteman A, Li Z. Comparisons between beam and continuum models for modelling wheel-rail impact at a singular rail surface defect. Int J Mech Sci 2021;198:106400.
[38] Dimitrovová Z. Two-layer model of the railway track: analysis of the critical velocity and instability of two moving proximate masses. Int J Mech Sci 2022;217:107042.
[39] Xu L, Chen X, Li X, He X. Development of a railway wagon-track interaction model: case studies on excited tracks. Mech Syst Signal Process 2018;100:877–98.
[40] Yang Z, Deng X, Li Z. Numerical modeling of dynamic frictional rolling contact with an explicit finite element method. Tribol Int 2019;129:214–31.
[41] Deng X, Qian Z, Li Z, Dollevoet R. Applicability of half-space-based methods to non-conforming elastic normal contact problems. Int J Mech Sci 2017;126:229–34.
[42] Yang Z, Boogaard A, Wei Z, Liu J, Dollevoet R, Li Z. Numerical study of wheel-rail impact contact solutions at an insulated rail joint. Int J Mech Sci 2018;138:310–22.
[43] Deng X, Li Z, Qian Z, Zhai W, Xiao Q, Dollevoet R. Pre-cracking development of weld-induced squats due to plastic deformation: five-year field monitoring and numerical analysis. Int J Fatigue 2019;127:431–44.
[44] Yang Z, Li Z. A numerical study on waves induced by wheel-rail contact. Int J Mech Sci 2019;161:105069.
[45] Mandal NK, Dhanasekar M. Sub-modelling for the ratchetting failure of insulated rail joints. Int J Mech Sci 2013;75:110–22.
[46] Su H, Pun CL, Mutton P, Kan Q, Kang G, Yan W. Numerical study on the ratcheting performance of rail flash butt welds in heavy haul operations. Int J Mech Sci 2021;199:106434.
[47] Yang Z, Li Z. Numerical modeling of wheel-rail squeal-exciting contact. Int J Mech Sci 2019;153:490–9.
[48] Lai VV, Chiello O, Brunel JF, Dufrenoy P. The critical effect of rail vertical phase response in railway curve squeal generation. Int J Mech Sci 2020;167:105281.
[49] Li Z, Li S, Zhang P, Núñez A, Dollevoet R. Mechanism of short pitch rail corrugation: initial excitation and frequency selection for consistent initiation and growth. Int J Rail Transp 2022. https://doi.org/10.1080/23248378.2022.2156402.
[50] Knothe K, Strzyzakowski Z, Willner K. Rail vibrations in the high frequency range. J Sound Vib 1994;169:111–23.
[51] Thompson D. Wheel-rail noise generation, part III: rail vibration. J Sound Vib 1993;161:421–46.
[52] Thompson D, Verheij J. The dynamic behaviour of rail fasteners at high frequencies. Appl Acoust 1997;52:1–17.

[53] Oregui M, De Man A, Woldekidan M, Li Z, Dollevoet R. Obtaining railpad properties via dynamic mechanical analysis. J Sound Vib 2016;363:460–72.
[54] Wei K, Wang F, Wang P, Liu ZX, Zhang P. Effect of temperature-and frequency-dependent dynamic properties of rail pads on high-speed vehicle–track coupled vibrations. Veh Syst Dyn 2017;55:351–70.
[55] Luo Y, Liu Y, Yin H. Numerical investigation of nonlinear properties of a rubber absorber in rail fastening systems. Int J Mech Sci 2013;69:107–13.
[56] Oregui M, Li Z, Dollevoet R. An investigation into the modeling of railway fastening. Int J Mech Sci 2015;92:1–11.
[57] Egana J, Vinolas J, Seco M. Investigation of the influence of rail pad stiffness on rail corrugation on a transit system. Wear 2006;261:216–24.
[58] Oyarzabal O, Gomez J, Santamaria J, Vadillo E. Dynamic optimization of track components to minimize rail corrugation. J Sound Vib 2009;319:904–17.
[59] Cui X, Chen G, Yang H, Zhang Q, Ouyang H, Zhu M. Study on rail corrugation of a metro tangential track with Cologne-egg type fasteners. Veh Syst Dyn 2016;54:353–69.
[60] Liu W, Zhang H, Liu W, Thompson DJ. Experimental study of the treatment measures for rail corrugation on tracks with Egg fasteners in the Beijing metro. Proc Inst Mech Eng Part F J Rail Rapid Transit 2018;232:1360–74.
[61] Zhang P, Li S, Núñez A, Li Z. Vibration modes and wave propagation of the rail under fastening constraint. Mech Syst Signal Process 2021;160:107933.
[62] Zhang P, Li S, Núñez A, Li Z. Multimodal dispersive waves in a free rail: numerical modeling and experimental investigation. Mech Syst Signal Process 2021;150:107305.
[63] Knothe K, Grassie S. Modelling of railway track and vehicle/track interaction at high frequencies. Veh Syst Dyn 1993;22:209–62.
[64] Hiensch M, Nielsen JC, Verheijen E. Rail corrugation in The Netherlands – measurements and simulations. Wear 2002;253:140–9.
[65] Benson DJ, Hallquist JO. A single surface contact algorithm for the post-buckling analysis of shell structures. Comput Methods Appl Mech Eng 1990;78:141–63.
[66] Zhao X, Li Z. The solution of frictional wheel–rail rolling contact with a 3D transient finite element model: validation and error analysis. Wear 2011;271:444–52.
[67] Yang Z, Boogaard A, Chen R, Dollevoet R, Li Z. Numerical and experimental study of wheel-rail impact vibration and noise generated at an insulated rail joint. Int J Impact Eng 2018;113:29–39.
[68] Molodova M, Li Z, Núñez A, Dollevoet R. Validation of a finite element model for axle box acceleration at squats in the high frequency range. Comput Struct 2014;141:84–93.
[69] Li Z, Zhao X, Dollevoet R, Molodova M. Differential wear and plastic deformation as causes of squat at track local stiffness change combined with other track short defects. Veh Syst Dyn 2008;46:237–46.
[70] Kalousek J, Johnson K. An investigation of short pitch wheel and rail corrugations on the Vancouver mass transit system. Proc Inst Mech Eng Part F J Rail Rapid Transit 1992;206:127–35.
[71] Neilsen J. Evolution of rail corrugation predicted with a non-linear wear model. J Sound Vib 1999;227:915–33.
[72] Oregui M, Li Z, Dollevoet R. Identification of characteristic frequencies of damaged railway tracks using field hammer test measurements. Mech Syst Signal Process 2015;54:224–42.
[73] Thompson D. Experimental analysis of wave propagation in railway tracks. J Sound Vib 1997;203:867–88.
[74] Heliot C. Small-scale test method for railway dynamics. Veh Syst Dyn 1986;15:197–207.
[75] Naeimi M, Li Z, Petrov RH, Sietsma J, Dollevoet R. Development of a new downscale setup for wheel-rail contact experiments under impact loading conditions. Exp Tech 2018;42:1–17.
[76] Zhang P, Moraal J, Li Z. Design, calibration and validation of a wheel-rail contact force measurement system in V-Track. Measurement 2021;175:109105.
[77] Oregui M, Li Z, Dollevoet R. An investigation into the vertical dynamics of tracks with monoblock sleepers with a 3D finite-element model. Proc Inst Mech Eng Part F J Rail Rapid Transit 2016;230:891–908.
[78] Yang Z, Zhang P, Wang L. Wheel-rail impact at an insulated rail joint in an embedded rail system. Eng Struct 2021;246:113026.
[79] Wang Y, Wu T. The growth and mitigation of rail corrugation due to vibrational interference between moving wheels and resilient track. Veh Syst Dyn 2020;58:1257–84.
[80] Cui X, He Z, Huang B, Chen Y, Du Z, Qi W. Study on the effects of wheel-rail friction self-excited vibration and feedback vibration of corrugated irregularity on rail corrugation. Wear 2021;477:203854.